Chinese Journal of Catalysis 53 (2023) 134–142

available at www.sciencedirect.com

ScienceDirect

journal homepage: www.sciencedirect.com/journal/chinese-journal-of-catalysis

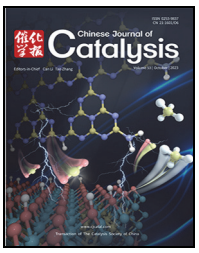

Article

# High-valence metal-doped amorphous $IrO_x$ as active and stable electrocatalyst for acidic oxygen evolution reaction

Ning Zhang [a,b], Jiayi Du [a,b], Na Zhou [a,b], Depeng Wang [a,b], Di Bao [a,*], Haixia Zhong [a,b,*], Xinbo Zhang [a,b,*]

[a] *State Key Laboratory of Rare Earth Resource Utilization, Changchun Institute of Applied Chemistry, Chinese Academy of Science, Changchun 130022, Jilin, China*

[b] *School of Applied Chemistry and Engineering, University of Science and Technology of China, Hefei 230026, Anhui, China*

ARTICLE INFO

*Article history:*
Received 30 May 2023
Accepted 6 September 2023
Available online 25 October 2023

*Keywords:*
Acidic oxygen evolution reaction
High-valence metal doping
Iridium oxide
Oxygen defect
Electrocatalysis

ABSTRACT

Proton-exchange membrane water electrolysis, particularly driven by renewable electricity, is a sustainable strategy for green hydrogen production. However, developing highly active and stable electrocatalysts to accelerate the oxygen evolution reaction (OER) remains challenging. Herein, we introduce an effective strategy for constructing high-valence metal-doped $IrO_x$ with abundant oxygen vacancies, while simultaneously enhancing the catalytic activity and stability of the acidic OER. The synthesized Ta-doped $IrO_x$ (350-Ta@$IrO_x$) exhibits ultramicroscopic nanoparticle morphology and abundant surface oxygen vacancies, enabling a rapid OER process with a low overpotential of 223 mV at 10 mA $cm^{-2}$ and 147.7 times higher mass activity (1207.4 A $g_{Ir}^{-1}$) than that of commercial $IrO_2$ at 1.55 V versus the reversible hydrogen electrode. More importantly, 350-Ta@$IrO_x$ affords excellent stability with insignificant potential degradation after 500 h of electrolysis at 10 mA $cm^{-2}$, originating from the low operating potential and suppressed dissolution and oxidation of oxygen vacancy active sites *via* Ta doping. Density functional theory calculations suggest that Ta doping and oxygen defect engineering are effective in facilitating the nucleophilic attack of water molecules, thereby accelerating the rate-determining step toward high catalytic OER activity on Ta-doped $IrO_x$. We anticipate that this study will provide an effective method to obtain active and stable electrocatalysts *via* high-valence metal doping.



## 1. Introduction

Hydrogen has been regarded as a potential energy carrier instead of fossil fuels, addressing energy demand and environmental issues [1]. Water splitting, powered by renewable electricity from wind or solar energy, is attractive for green hydrogen production because of its high efficiency and cost-effectiveness [2–4]. Among the innovative pathways, polymer electrolyte membrane water electrolysis (PEMWE) is a promising alternative owing to its high operating current densities, hydrogen purity, and fast system response [5–7]. However, its efficiency is limited by the sluggish kinetics of the electrochemical reactions [8,9]. Compared with the cathodic hydrogen evolution reaction (HER), which is a two-electron transfer process [10], the anodic oxygen evolution reaction (OER) involves considerably more complex steps in the

* Corresponding author. E-mail: xbzhang@ciac.ac.cn (X. Zhang), hxzhong@ciac.ac.cn (H. Zhong), dbao@ciac.ac.cn (D. Bao).
This work was supported by the National Key R&D Program of China (2020YFE0204500), the National Natural Science Foundation of China Outstanding Youth Science Foundation of China (Overseas), the National Natural Science Foundation of China (52071311, 52273277, 52072362, 21905269), Jilin Province Science and Technology Development Plan Funding Project (20220201112GX) and Youth Innovation Promotion Association CAS (2021223).
https://doi.org/10.1016/S1872-2067(23)64517-6

four-electron transfer process, imposing an urgent requirement for effective electrocatalysts [11,12]. In recent years, considerable efforts have been made in improving the catalytic activity of OER electrocatalysts such as Ce-doping of $IrO_2$ [13] and Ir-based perovskite oxide [14,15]. However, these electrocatalysts remain unstable owing to their high applied potentials and corrosive electrolytes [16]. Therefore, extensive research is required to simultaneously enhance the activity and stability of OER electrocatalysts toward high-efficiency and low-cost PEMWE [17].

Amorphous hydrated $IrO_x$-type electrocatalysts are considered as potential OER candidates with high catalytic performance in acidic media [18,19]. Typically, amorphous $IrO_x$ can be obtained by the dynamic surface reconstruction of transition-metal-mixed iridium oxides [20,21], particularly with rare-earth elements [22], because of their thermodynamic instability under acidic conditions. Moreover, alkali metal intercalation [23,24] by thermal treatment can be used to synthesize amorphous $IrO_x$. In addition, $IrO_x$ can be prepared using a low-temperature sintering method that converts iridium chloride into incompletely oxidized iridium oxide [25]. These $IrO_x$ electrocatalysts with abundant oxygen defects [26] contribute to the reduced Ir valence state and weakened Ir–O binding. These electrophilic oxygen defects of $IrO_x$ are conducive to nucleophilic attack by water, resulting in a significant enhancement in the catalytic activity. Generally, the adsorption of water by the defects has a low activation energy and is considered the source of the high activity of the amorphous oxide structure. The weakened binding between iridium and oxygen accelerates the dissolution of Ir without electron transfer ($Ir^{III}_{(oxide)}$ to $Ir^{3+}_{(aq)}$) [27] during the acidic OER, inducing inferior stability. In most cases, the enhanced activities of Ir-based electrocatalysts are negatively correlated with their stability through an Ir dissolution process during the acidic OER [28]. Few studies have aimed to improve the stability of amorphous $IrO_x$ while maintaining its high catalytic activity. However, most studies have focused on improving the catalytic activity of amorphous $IrO_x$, and only a few studies have aimed at improving its stability. Doping is generally employed to boost the activity and stability of electrocatalysts by regulating the negatively charged states on nearby O sites or by tuning the electronic structures of metal oxides [29,30]. For example, Fe-doped NiOOH successfully enables efficient and stable OER electrocatalytic reactions in alkaline electrolytes [31]. Moreover, high-valence transition-metal doping, with elements such as Hf [32], Re [33], W [34], and Ta [35–37], not only regulates the electronic structure of the catalytic center by accepting electrons, but also stabilizes these catalytic centers owing to their corrosion resistance and strong metal–O bonds. Inspired by these results, high-valence metal doping is expected to enhance the activity of amorphous $IrO_x$ and reinforce its structural stability toward the acidic OER.

Herein, using the high-valence metal (Ta) doping strategy through a facile molten salt sintering method, we developed Ta-doped amorphous hydrated $IrO_x$ (Ta@$IrO_x$) with abundant oxygen vacancies as highly active and stable electrocatalysts for acidic OER. As an electron-accepting dopant, Ta optimized the structural morphology and generated surface oxygen vacancies over $IrO_x$. The resultant 350-Ta@$IrO_x$ exhibited a high acidic OER activity with a low overpotential of 223 mV at 10 mA $cm^{-2}$, largely surpassing the commercial $IrO_2$. Combined with density functional theory (DFT) calculations, Ta-doped $IrO_x$ enabled a rapid electrocatalytic OER by effectively promoting the nucleophilic attack of the $H_2O$ molecule and reducing the energy barriers of the rate-determining step (RDS). Importantly, 350-Ta@$IrO_x$ exhibited no obvious potential degradation under 500 h operation at 10 mA $cm^{-2}$, owing to the suppressed dissolution of Ir and oxidation of active defects *via* Ta doping. This study sheds light on the development of active and stable amorphous $IrO_x$ *via* high-valence metal doping.

## 2. Experimental

### 2.1. Chemicals

All the chemicals, including $NaNO_3$ (99.9%), $IrCl_3{\cdot}xH_2O$ (99%), $TaCl_5$ (99.9%), $H_2SO_4$, $C_3H_8O$, and commercial $IrO_2$ were purchased from Aladdin Chemical Reagent Co, Ltd. Deionized water (18 MΩ $cm^{-1}$) was used to prepare all aqueous solutions. The commercial IrOx ($IrO_2{\cdot}2H_2O$, 99.95% metals basis) was purchased from Sigma-Aldrich. All reagents were of analytical grade and used without further purification.

### 2.2. Preparation of $IrO_x$ and Ta@$IrO_x$ series electrocatalysts

350-Ta@$IrO_x$ was synthesized using a modified Adams fusion method [38]. Metal precursors (1 mmol of $TaCl_5$ and 9 mmol of $IrCl_3{\cdot}xH_2O$) and excess $NaNO_3$ (10 g) were added to 10 mL of water, and a homogeneous aqueous solution was prepared *via* stirring and heating. The solvent was then evaporated from the solution and the obtained solid mixture was ground carefully. Subsequently, the ground powder was further calcinated at a specified temperature for 2 h at a heating rate of 1.7 °C $min^{-1}$. After a quick cooling to room temperature, washing with water, dilution with $H_2SO_4$ solution, and freeze-drying, the Ta-doped $IrO_x$ electrocatalyst sintered at 350 °C was obtained and named 350-Ta@$IrO_x$. These samples prepared under various pyrolysis temperatures (350, 400, 450 °C) with and without Ta doping were named as 350-Ta@$IrO_x$, 400-Ta@$IrO_x$, 450-Ta@$IrO_x$, 350-$IrO_x$, 400-$IrO_x$, and 450-$IrO_x$.

### 2.3. Conventional characterizations

The size and morphology were characterized by field-emission scanning electron microscopy (SEM, Hitachi S-4800) at 20 kV and transmission electron microscopy (TEM, Tecnai G2 F20) at an acceleration voltage of 200 kV. X-ray diffraction (XRD) patterns were collected using a Rigaku micro-XRD with Cu $K_\alpha$ radiation (40 kV, 15 mA, $\lambda$ = 1.5418 Å), recorded with 2$\theta$ ranging from 20° to 80°. The bonding configurations of the samples were determined by X-ray photoelectron spectroscopy (XPS, Shimadzu AXIS Supra). The binding energies were corrected based on the carbon peak at 284.8 eV. The concentration of the metal ions in the electrolyte was analyzed by inductively coupled plasma-mass spectroscopy

(ICP-MS, Thermo iCAP 7400). All the electrochemical test data were measured using an electrochemical workstation (Bio-Logic VMP-3). Electron paramagnetic resonance (EPR) patterns were recorded using an electron spin resonance spectrometer (JEOL, JES-FA200).

### 2.4. Electrochemical measurements

#### 2.4.1. Electrodes preparation

Typically, 10 mg of electrocatalysts were dispersed in 2 mL of mixed solvent with water and isopropanol (1:3, *v*:*v*), and 100 μL of 5 wt% Nafion solution was added into this mixture. The resulting solution was ultrasonicated for at least 30 min until a well-dispersed ink was obtained. The ink was dropped onto glassy carbon or carbon paper at an electrocatalyst load of ~0.2 mg $cm^{-2}$.

#### 2.4.2. Three-electrode system measurements

Electrochemical measurements of the prepared electrocatalysts were performed in 0.5 mol $L^{-1}$ $H_2SO_4$ *via* a standard three-electrode system at room temperature. Platinum mesh and saturated Ag/AgCl electrodes were used as counter and reference electrodes, respectively. A catalyst-coated rotating disk electrode (RDE, diameter: 5.61 mm, electrode surface area: 0.2475 $cm^2$, Pine Research Instrument) or carbon paper was used as the working electrode (electrode surface area: 0.5 $cm^2$). The polarization curves were normalized to the surface area of the electrode. The saturated Ag/AgCl reference electrode was calibrated using a reversible hydrogen electrode (RHE), as described in a previous report (Fig. S1) [39], and the resulting potential of zero net current was found to be –0.213 V in 0.5 mol $L^{-1}$ $H_2SO_4$. Before each test, oxygen was injected into the electrolyte for 20 min.

The RDE was used as the working electrode at a rotation speed of 1600 rpm. The electrocatalyst was activated before each electrochemical measurement, as described in previous report [40]. Linear sweep voltammetry (LSV) curves were recorded at a scan rate of 10 mV $s^{-1}$ with capacitance correction and 80% Ohmic drop correction. The Tafel plots were constructed by sweeping the electrode potential from high to low across a linear Tafel region. Electrochemical AC impedance spectroscopy (EIS) measurements were performed in the frequency range of 0.2–100 MHz at 1.513 V *vs.* RHE. The electrochemical double-layer capacitances ($C_{dl}$) of the catalysts were assessed by cyclic voltammetry (CV) at various scan rates from 5 to 25 mV $s^{-1}$. $C_{dl}$ values were calculated according to the linear relationship between the current density and the scanning speed based on the equation, $i = \nu C_{dl}$ [41].

Electrocatalyst-coated carbon paper was used as the working electrode for stability tests. Chronopotentiometry (CP) was performed at a constant current density of 10 mA $cm^{-2}$ in 0.5 mol $L^{-1}$ $H_2SO_4$ at room temperature.

### 2.5. DFT method

All computational tasks in this study were performed using the software PWmat [42,43]. The plane wave cutoff energy was 50 Ry, and the Perdew-Burke-Ernzerhof exchange-correlation functional was applied [44]. The force convergence was set to 0.02 eV $Å^{-1}$. To simulate the OER on the surface of the electrocatalysts, slab models of a 2 × 3 supercell of $IrO_2$ with doped Ta or oxygen vacancies were constructed with exposed (110) facets. The vacuum layer in the z direction was set to 15 Å to avoid the periodic effect. The van der Waals correction was also considered using DFT-D3 [45–47]. A Monkhorst-Park 3 × 4 × 1 K-point grid of the Brillouin zone was used for cell relaxation.

## 3. Results and discussion

### 3.1. Synthesis and morphology characterization

350-Ta@$IrO_x$ was prepared using a one-step sintering-modified Adams molten salt method [38], and the low calcination temperature of this method favored the formation of ultrasmall amorphous hydrated iridium oxide nanoparticles. As shown in Fig. S2, 350 °C is chosen as the minimum phase formation temperature from the metal precursors to iridium oxide, which is consistent with the melting point of $NaNO_3$ (307 °C).

The SEM images of commercial $IrO_2$ and the prepared electrocatalysts with and without Ta doping at various temperatures are shown in Figs. S3 and S4. The results show that 350-Ta@$IrO_x$ has a lamellar morphology that is very different from that of pure rutile $IrO_2$. As shown in Fig. 1(a), the low-resolution TEM image of 350-Ta@$IrO_x$ confirms the lamellar structure consisting of ultra-small nanoparticles, which is due to the nucleation and growth of iridium oxide nanoparticles on the surface of sodium nitrate. When increasing the pyrolysis temperature from 350 to 450 °C, large-sized iridium oxide bulk with less lamellar structure was generated due to the Ostwald ripening of iridium oxide under high temperatures (Figs. S5–S10). The formation of a lamellar or porous structure originates from the quick cooling operation, and the removed molten $NaNO_3$ is solidified by water. The transformation of the structure *via* the Ostwald ripening process upon increasing the temperature resulted in the generation of larger nanoparticles and higher crystallinity of the iridium oxide, which was con-

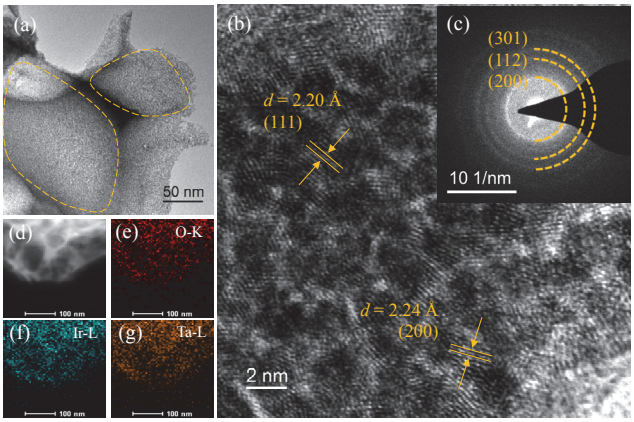


**Fig. 1.** Morphology characterization of 350-Ta@$IrO_x$. (a) TEM image; (b) HR-TEM image with lattice spacing; (c) SAED image; (d–g) Elemental mapping images.

sistent with the results of a previous study [48]. Notably, Ta-doping samples better maintained the porous morphology than the undoped samples at the same pyrolysis temperature, suggesting a stabilizing effect of heteroelement doping on the microscopic morphology under high calcination temperatures.

High-resolution TEM (HR-TEM) was used to investigate the nanostructure of 350-Ta@$IrO_x$. As shown in Fig 1(b), ultrasmall particles with diameters of approximately 2 nm are observed with the clear lattice spacing of 2.20 and 2.24 Å, which are ascribed to the (111) and (200) facets of rutile $IrO_2$ (ICDD-PDF: 97-064-0887) with slightly stray due to the abundant oxygen defects. As shown in Fig. 1(c), the selected area electron diffraction (SAED) pattern shows the (301), (112), and (200) diffraction rings of rutile $IrO_2$, implying that 350-Ta@$IrO_x$ has a polycrystalline structure [49]. The particle size of Ta@$IrO_x$ (Figs. S5–S10) increases and its crystallinity improves with the increase in sintering temperature. Notably, the nanocrystal size of the Ta-doped samples is significantly smaller than that of the undoped samples at the same temperature. In addition, the dopant increases the temperature of crystal formation and induces low crystallinity of $IrO_x$ at a similar synthesis temperature. Consequently, the particles of 350-Ta@$IrO_x$ are smaller than those of 350-$IrO_x$. The TEM images of commercial $IrO_2$ are shown in Fig. S11.

TEM coupled with energy-dispersive X-ray spectroscopy (TEM-EDX) analysis of the Ta-doped samples was performed. As shown in Figs. 1 (d)–(g), Figs. S7 (c)–(f) and Figs. S9 (c)–(f), the images confirm the homogeneous distribution of Ir, Ta, and O over all the Ta@$IrO_x$ electrocatalysts. Combined with ICP-MS analysis (Table S1), it is verified that the actual ratios of Ir and Ta in 350-Ta@$IrO_x$ are close to the nominal ratios (9:1 molar ratio) in the precursor mixtures. The crystal structures of the prepared samples are examined by XRD, as shown in Fig. 2(a) and Fig. S12. The sharp diffraction peaks of commercial $IrO_2$ at 28.0°, 34.8°, and 54.1° are assigned to the single rutile $IrO_2$ phase. The XRD patterns of 350-Ta@$IrO_x$, 400-Ta@$IrO_x$, and 350-$IrO_x$ display two broad peaks at approximately 30° and 60°, which are attributed to the ultrafine Ir oxide nanocrystals. However, typical peaks of both rutile-type $IrO_2$ and tantalum oxide are observed for 450-Ta@$IrO_x$ because of phase separation at elevated pyrolysis temperatures. Notably, 400-$IrO_x$ has two imperceptible peaks attributed to rutile $IrO_2$, signifying the critical role of Ta in the synthesis of amorphous iridium oxide nanoparticles. In summary, the XRD results indicate that Ta doping and a low pyrolysis temperature synergistically favor the formation of $IrO_x$ instead of highly crystalline $IrO_2$.

XPS was used to probe the surface chemical composition and valence states of the prepared electrocatalysts. The survey scan spectra (Fig. S13) verified the presence of Ta, Ir, and O in all the Ta-doped samples, indicating the successful Ta doping of 350-Ta@$IrO_x$. Notably, the absence of the signals of Na 1*s* (1071.4 eV), N 1*s* (407.4 eV), and C 1*s* (200.0 eV) for all the prepared samples because of the removal of $NaNO_3$ and chloride *via* acidic washing, combined with the ICP analysis (Table S1), excluded the possible role of Na, N, or Cl in enhancing the electrocatalytic performance. Two sets of doublets with binding

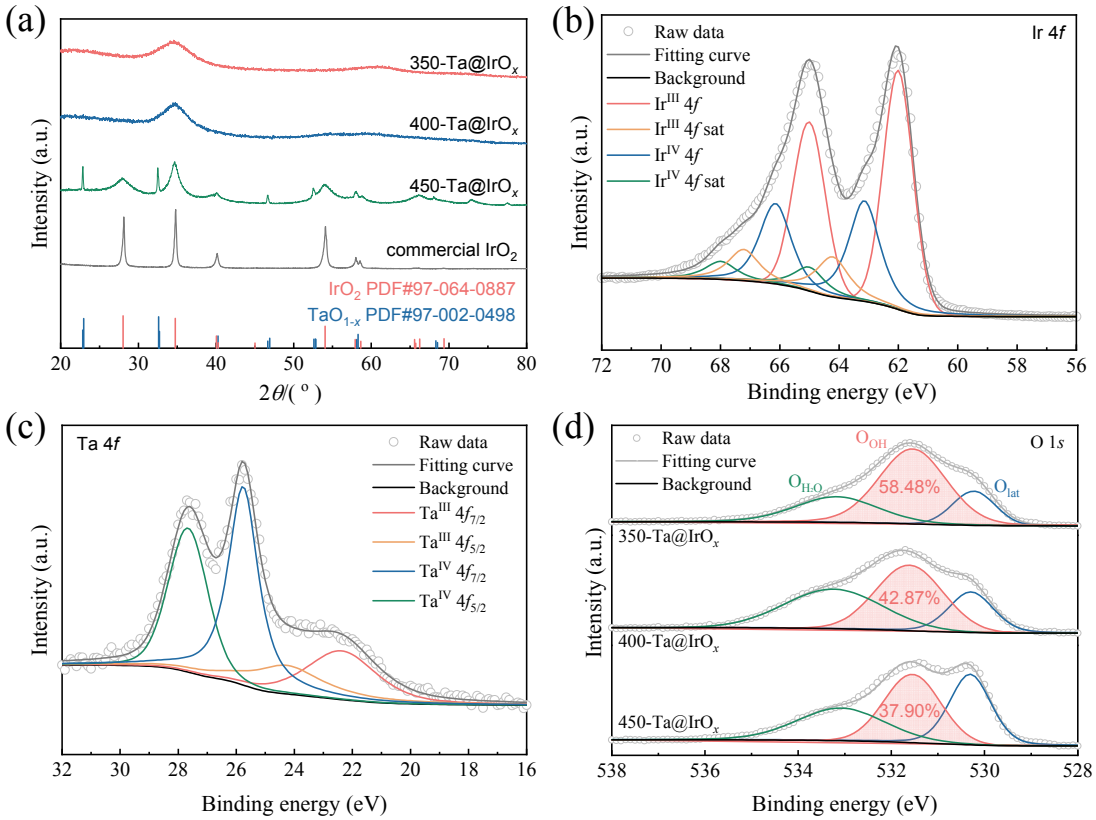


**Fig. 2.** (a) XRD patterns of Ta@$IrO_x$ electrocatalysts and commercial $IrO_2$. (b) Ir 4*f* XPS spectra of 350-Ta@$IrO_x$. (c) Ta 4*f* XPS spectra of 350-Ta@$IrO_x$. (d) O 1*s* XPS spectra of 350-Ta@$IrO_x$, 400-Ta@$IrO_x$, and 450-Ta@$IrO_x$.

energies at 62.0 and 65.0 eV, and 63.1, and 66.1 eV in the high-resolution Ir 4*f* XPS spectra of 350-Ta@IrO$_x$ (Fig. 2(b)) implied that $Ir^{3+}$ and $Ir^{4+}$ co-existed on 350-Ta@IrO$_x$. For the Ta 4*f* spectra (Fig. 2(c) and Fig. S14), the doublets signals at 22.37 and 24.27 eV, and 25.76 and 27.66 eV indicated the presence of $Ta^{3+}$ and $Ta^{4+}$, respectively, in 350-Ta@IrO$_x$, 400-Ta@IrO$_x$, and 450-Ta@IrO$_x$ [35]. As the pyrolysis temperature increased, the proportion of $Ta^{3+}$ content also increased, corresponding to phase separation at higher pyrolysis temperatures. As shown in Fig. 2(d), the O 1*s* XPS spectra can be deconvoluted into three peaks: the oxygen in adsorbed water ($O_{H2O}$) at 533.2 eV, lattice oxygen ($O_{lat}$) at 530.2 eV, and coordinatively unsaturated oxygen or oxygen in hydroxyl group at 531.5 eV. Generally, the XPS signal of $O_{OH}$ is considered proportional to the oxygen defects [50], which induce the unsaturated coordination of Ir as active sites for the OER. The peak fit data of the O 1s XPS signal for all electrocatalyst samples are summarized in Table S2. The peak area percentages of $O_{OH}$ relative to $O_{lat}$ for 350-Ta@IrO$_x$, 400-Ta@IrO$_x$, and 450-Ta@IrO$_x$ are 58.48%, 42.87%, and 37.90%, respectively, suggesting that the number of oxygen defects decreases with increasing calcination temperature. Similarly, the contents of $O_{OH}$ species in the un-doped samples for 350-IrO$_x$, 400-IrO$_x$, and 450-IrO$_x$ are 55.16%, 47.80%, and 43.88%, respectively, as shown in Fig. S15 and Table S2. Thus, electrocatalysts obtained at low oxidation temperatures have more oxygen defects, which can effectively promote electrocatalytic reactions [48]. Increasing the pyrolysis temperature also induces a relative increase in the Ir valence states of these IrO$_x$ samples, as verified by the positive shift of the binding energy for the Ir 4*f* peaks (Fig. S16 and Table S3), owing to the facile formation of crystalline $IrO_2$ with fewer oxygen defects at high oxidation temperatures. However, an insignificant shift is observed as the temperature increases from 350, 400, to 450 °C owing to the electron-constraining effect of the high-valent metal Ta, which minimizes the change in the valence state of Ir (Fig. S17). Furthermore, EPR spectrum shown in Fig. S18 confirms that the oxygen defects are attributed to oxygen vacancies. Therefore, Ta-doping and low pyrolysis temperatures enable the effective optimization of the electronic structures and induce abundant oxygen vacancies in the electrocatalysts, which can boost the acidic OER activity. Furthermore, the activities of the oxygen species in 350-Ta@IrO$_x$ and commercial $IrO_2$ were analyzed by $H_2$-TPR (temperature-programmed reduction. As shown in Fig. S19, 350-Ta@IrO$_x$ exhibits a lower reduction temperature with $H_2$ at 102 °C, revealing that the O species are more reactive in 350-Ta@IrO$_x$.

### 3.2. Electrochemical acidic OER analysis

The acidic OER performance of all the prepared electrocatalysts and commercial $IrO_2$ was evaluated using the RDE technique in a 0.5 mol $L^{-1}$ $H_2SO_4$ electrolyte. As shown in Fig. 3(a), 350-Ta@IrO$_x$ only requires a lower overpotential (223 mV) than that of commercial $IrO_2$ (440 mV) to achieve a benchmark current density of 10 mA $cm^{-2}$. In contrast, 400-Ta@IrO$_x$ and 450-Ta@IrO$_x$ exhibit overpotentials of 245 and 268 mV, respectively, at identical current densities. These results indicate that more oxygen vacancies and smaller particle sizes due to lower pyrolysis temperatures significantly enhance the OER activity. The OER activities of the undoped electrocatalysts are shown in Fig. S20. The electrocatalytic activities of all samples follow the order: 350-Ta@IrO$_x$ > 350-IrO$_x$ > 400-TaF@IrO$_x$ > 400-IrO$_x$ > 450-Ta@IrO$_x$ > 450-IrO$_x$ > commercial $IrO_2$, indicating that a combination of low pyrolysis temperature and Ta doping optimizes the OER activity of IrO$_x$. In addition, 350-Ta@IrO$_x$ exhibits higher activity than its commercial counterparts (commercial $IrO_2$ and commercial IrO$_x$), as shown in Fig. S21. Among the 350-Ta@IrO$_x$ samples with various Ta contents in the precursor, the sample with 5% doping exhibits the highest OER activity, as shown in Fig. S22. Furthermore, as

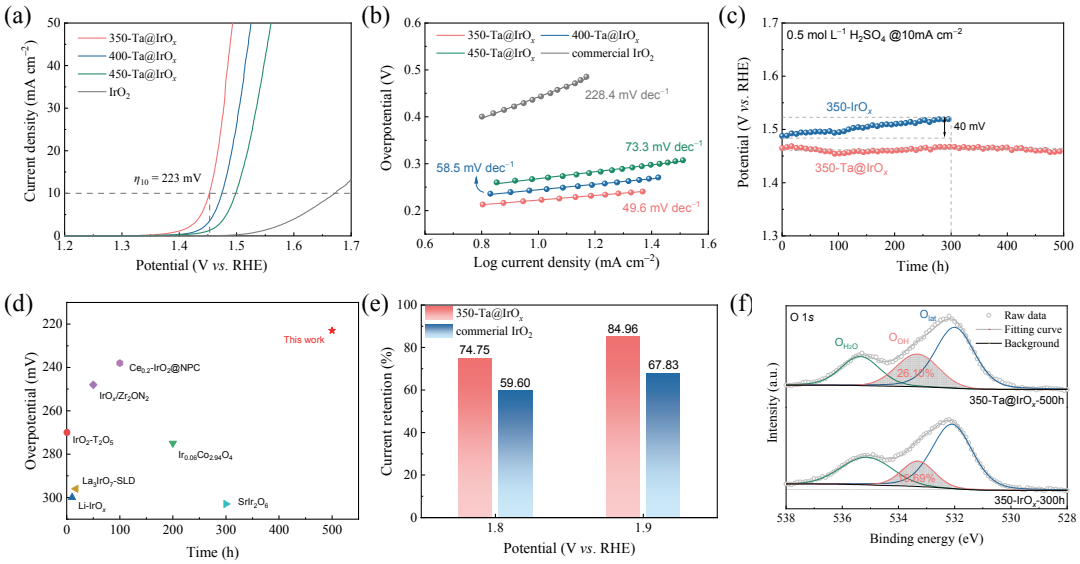


**Fig. 3.** (a) LSV curves of 350-Ta@IrO$_x$, 400-Ta@IrO$_x$, 450-Ta@IrO$_x$, and commercial $IrO_2$. (b) Tafel slope plots. (c) CP curves of 350-Ta@IrO$_x$ and 350-IrO$_x$. (d) Comparisons of 350-Ta@IrO$_x$ with other representative acidic OER electrocatalysts. (e) Current retention of 350-Ta@IrO$_x$ and commercial $IrO_2$ after the OER. (f) XPS spectra of 350-Ta@IrO$_x$ and 350-IrO$_x$ after the OER.

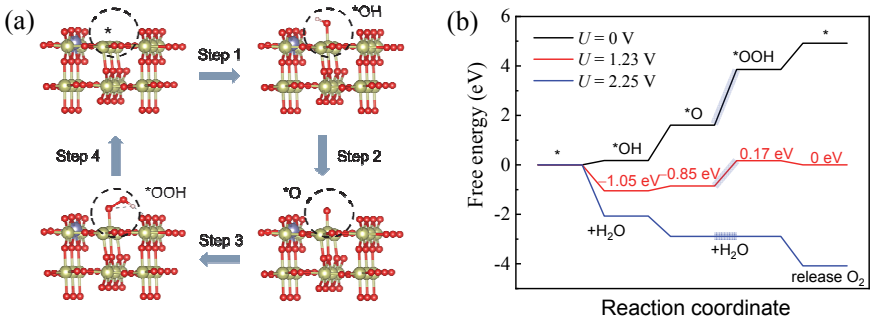


**Fig. 4.** (a) Four-step OER proceeding through the formation of *OH, *O, and *OOH on Ta-doped $IrO_x$. (b) Predicted free energy profiles of acidic OER on Ta-doped $IrO_x$ (* denotes the active site of the catalyst).

shown in Fig. S23, 350-Ta@$IrO_x$ exhibits a significantly higher mass activity of 1207.4 A $g_{Ir}^{-1}$ at 1.55 V *vs.* RHE compared with the counterparts, highlighting the effectiveness of Ta doping in enhancing the intrinsic activity of Ir.

The OER kinetics were investigated by analyzing the Tafel slopes. As shown in Fig 3(b), the Tafel slopes of 350-Ta@$IrO_x$, 400-Ta@$IrO_x$, and 450-Ta@$IrO_x$ are 49.6, 58.5, and 73.3 mV $dec^{-1}$, respectively, all of which are smaller than that of the benchmark commercial $IrO_2$ (228.4 mV $dec^{-1}$), demonstrating their accelerated reaction kinetics compared with commercial $IrO_2$. Moreover, Ta-doped samples exhibit lower Tafel slope values than those of 350-$IrO_x$, 400-$IrO_x$, and 450-$IrO_x$ (57.3, 66.4, and 75.4 mV $dec^{-1}$, respectively) (Fig. S24), indicating the positive role of Ta doping in promoting the acidic OER on amorphous $IrO_x$ electrocatalysts.

The $C_{dl}$ values of all the prepared samples was estimated using CV curves measured at various scan rates to evaluate their electrochemically active surface areas (Fig. S25). The most active 350-Ta@$IrO_x$ exhibits the highest $C_{dl}$ value of 192.2 mF $cm^{-2}$, suggesting its largest electrochemical active surface area with more active sites. EIS spectra recorded at 1.513 V *vs.* RHE are shown in Figs. S26 and S27. 350-Ta@$IrO_x$ exhibits the smallest charge transfer resistance among the relevant electrocatalyst samples and commercial $IrO_2$, which is favorable for fast acidic OER processes.

To evaluate the stability of the electrocatalysts toward practical applications, CP was performed in 0.5 mol $L^{-1}$ $H_2SO_4$ at 10 mA $cm^{-2}$, wherein carbon paper with electrocatalyst loading was used as the working electrode. As shown in Fig. 3(c), no noticeable increase in the potential is observed for 350-Ta@$IrO_x$ upon continuous operation for 500 h. However, the 350-$IrO_x$ electrocatalyst without Ta doping suffers from a distinct potential increase of 40 mV, even under a shorter operation time (300 h), suggesting the significant role of Ta in enhancing the stability of amorphous $IrO_x$ electrocatalysts. As shown in Fig. S28, commercial $IrO_2$ exhibits a sharp potential increase of ~100 mV after only 50 h of operation, which is due to the high applied potential required to achieve a current density of 10 mA $cm^{-2}$ and its poor stability in the acidic electrolyte, highlighting the long-term stability of 350-Ta@$IrO_x$ and 350-$IrO_x$. The 350-Ta@$IrO_x$ exhibits competitive electrochemical performance in terms of activity and stability compared with other representative electrocatalysts for the OER in acidic media (Fig. 3(d)). Additionally, the electrolysis at the high operation potential of 1.8 and 1.9 V *vs.* RHE was applied on the 350-Ta@$IrO_x$ and commercial $IrO_2$ for 5 h to further estimate their durability (Fig. S29). Although 350-Ta@$IrO_x$ delivers a higher current density at an identical potential, less current degradation is achieved (Fig. 3(e)), illustrating the higher stability of 350-Ta@$IrO_x$ than commercial $IrO_2$ toward practical applications. According to the ICP data in Table S4, the Ir dissolution rate of 350-Ta@$IrO_x$ (0.141 ppb $h^{-1}$) is almost half of 350-$IrO_x$ (0.279 ppb $h^{-1}$), demonstrating the stabilizing and anti-corrosive effects of Ta doping. To further reveal the origin of the stability of 350-Ta@$IrO_x$, XPS, TEM, and XRD were performed to elucidate its corrosion resistance. The XPS results showed that the surface hydroxyl oxygen content of 350-Ta@$IrO_x$ and 350-$IrO_x$ after long-term tests decreased to 26.10% and 16.69%, respectively, suggesting that 350-Ta@$IrO_x$ maintained more oxygen active sites than 350-$IrO_x$, likely due to the strong Ta–O bonds [50], and their role in stabilizing the oxygen species during the OER process. In addition, the minimal change in the binding energy of the Ir 4*f* XPS spectra of 350-Ta@$IrO_x$ after the OER (Figs. S15 and S16) demonstrated the reduced formation of the high-valent iridium oxide layer and its higher structural stability than 350-$IrO_x$ during the OER process. Moreover, as shown in the TEM images, the corresponding FFT and XRD patterns (Figs. S31–S33), the porous lamellar microscopic morphology and polycrystalline structure of 350-Ta@$IrO_x$ after 500 h of OER and those of 350-$IrO_x$ after 300 h of OER are well maintained. This implies that Ta doping is conducive to stabilizing the $IrO_x$ morphology and effectively alleviating the oxidation and dissolution of the active sites.

### 3.3. *DFT calculations*

DFT calculations were performed to better understand the contributions of Ta doping and oxygen vacancies to the high OER activity of Ta-doped $IrO_x$. Based on the abovementioned detailed structural characterization, the thermodynamically stable rutile $IrO_2$ (110) facet [35] was selected as a model for these electrocatalysts (Ta-doped $IrO_x$, $IrO_x$, and Ta-doped $IrO_2$) (Figs. 4(a), S34(a), and S35(a)). Here, OER at the applied electrocatalysts proceeded through four consecutive proton and electron transfer steps coupling with forming these *OH, *O, and *OOH intermediates [23], respectively. As shown in Fig. 4(a), these four elementary steps on the catalytic surface include $H_2O$ dissociation (step 1), proton release (step 2), $H_2O$

nucleophilic attack (step 3), and $O_2$ molecule release (step 4). The relative free energies for generating various intermediates on the three electrocatalysts are investigated at different potentials (0, 1.23, and 2.25 V), as shown in Figs. 4(b), S34(b), and S35(b). The results show that the RDS associated with the highest energy uptake over all three electrocatalysts is the transformation from *O to *OOH, which is consistent with a previous study [51]. RDS for Ta-doped $IrO_x$ has the minimum energy barrier of 1.02 eV at the theoretical potential ($U$ = 1.23 V), which is lower than that of undoped $IrO_x$ (1.23 eV) and Ta-doped $IrO_2$ (1.16 eV) without oxygen vacancies. The RDS for these samples is the conversion of *O to *OOH because of its higher energy barrier compared with the other steps. 350-Ta@$IrO_x$ exhibits the lowest energy barrier (0.17 eV) for the conversion of *O to *OOH, compared with $IrO_x$ (0.61 eV, Fig. S34), and Ta-$IrO_2$ (0.55 eV, Fig. S35). In addition, the OER with Ta-doped $IrO_x$ at 2.25 V is thermodynamically downhill because the free energy values of these steps are negative. Combined with the experimental analysis, we speculate that incorporating Ta and oxygen vacancies into iridium oxide enables $IrO_x$ to promote the nucleophilic attack of the $H_2O$ molecule, thus reducing the energy barriers for forming the key intermediate in the RDS and accelerating the overall OER process.

## 4. Conclusions

In summary, we developed a high-valence metal (Ta)-doping strategy to prepare amorphous $IrO_x$ nanoparticles for simultaneously boosting the catalytic activity and stability of the acidic OER. The optimal 350-Ta@$IrO_x$ exhibited high activity with a low overpotential of 223 mV and excellent stability of 500 h at 10 mA $cm^{-2}$. Impressively, the 350-Ta@$IrO_x$ electrocatalyst afforded significantly higher intrinsic catalytic activity with 147.7 times mass activity than (1207.4 A $g_{Ir}^{-1}$) that of commercial $IrO_2$. DFT studies revealed that Ta doping and defect engineering played important roles in enhancing the high activity of $IrO_x$ by promoting the nucleophilic attack of $H_2O$ molecules and reducing the energy barriers of the RDS. In addition, Ta doping stabilized the oxygen vacancy structure and effectively alleviated the oxidation and dissolution of Ir, thereby contributing to the long-term stability of 350-Ta@$IrO_x$. Our work points toward an effective design principle for rational activity and stability enhancement in electrocatalysts with high-valence metal doping engineering, and provides an insightful understanding of electrocatalyst deactivation.

## Conflict of interests

The authors declare that they have no known competing financial interests or personal relationships that could have appeared to influence the work reported in this paper.

## Electronic supporting information

Supporting information is available in the online version of this article.

## References


[1] J. A. Turner, *Science*, **2004**, 305, 972–974.
[2] Q. Xu, L. Zhang, J. Zhang, J. Wang, Y. Hu, H. Jiang, C. Li, *EnergyChem*, **2022**, 4, 100087.
[3] N. Du, C. Roy, R. Peach, M. Turnbull, S. Thiele, C. Bock, *Chem. Rev.*, **2022**, 122, 11830–11895.
[4] M. Tahir, L. Pan, F. Idrees, X. W. Zhang, L. Wang, J. J. Zou, Z. L. Wang, *Nano Energy*, **2017**, 37, 136–157.
[5] Z. C. Chen, L. Guo, L. Pan, T. Q. Yan, Z. X. He, Y. Li, C. X. Shi, Z. F. Huang, X. W. Zhang, J. J. Zou, *Adv. Energy Mater.*, **2022**, 12, 2103670.
[6] M. F. Lagadec, A. Grimaud, *Nat. Mater.*, **2020**, 19, 1140–1150.
[7] Z. Shi, J. Li, J. Jiang, Y. Wang, X. Wang, Y. Li, L. Yang, Y. Chu, J. Bai, J. Yang, J. Ni, Y. Wang, L. Zhang, Z. Jiang, C. Liu, J. Ge, W. Xing, *Angew. Chem. Int. Ed.*, **2022**, 61, e202212341.
[8] L. Li, P. Wang, Q. Shao, X. Huang, *Adv. Mater.*, **2021**, 33, 2004243.
[9] J. Yin, J. Jin, M. Lu, B. Huang, H. Zhang, Y. Peng, P. Xi, C. H. Yan, *J. Am. Chem. Soc.*, **2020**, 142, 18378–18386.
[10] B. Lu, C. B. Wahl, X. K. Lu, M. E. Sweers, H. Li, V. P. Dravid, L. C. Seitz, *J. Am. Chem. Soc.*, **2022**, 144, 13547–13555.
[11] R. Huang, Y. Z. Wen, H. S. Peng, B. Zhang, *Chin. J. Catal.*, **2022**, 43,


### Graphical Abstract

*Chin. J. Catal.*, 2023, 53: 134–142 doi: 10.1016/S1872-2067(23)64517-6

**High-valence metal-doped amorphous $IrO_x$ as active and stable electrocatalyst for acidic oxygen evolution reaction**

Ning Zhang, Jiayi Du, Na Zhou, Depeng Wang, Di Bao *, Haixia Zhong *, Xinbo Zhang *
*Changchun Institute of Applied Chemistry, Chinese Academy of Science; University of Science and Technology of China*

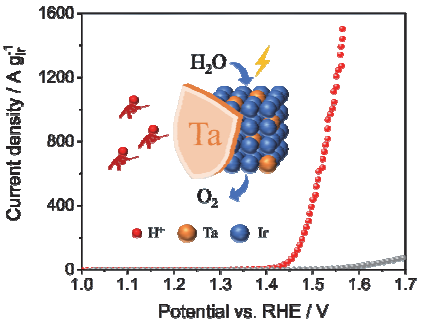


High-valence metal doping strategy is effective for developing efficient and stable $IrO_x$ electrocatalysts for acidic oxygen evolution reactions. The optimized electrocatalyst (350-Ta@$IrO_x$) exhibits higher mass activity and structural stability, benefiting from the regulation of the electronic structure and strong metal-oxygen bonds.

130–138.
[12] Q. Yao, J. B. Le, S. Z. Yang, J. Cheng, Q. Shao, X. Q. Huang, *Chin. J. Catal.*, **2022**, 43, 1493–1501.
[13] Y. Wang, S. Hao, X. Liu, Q. Wang, Z. Su, L. Lei, X. Zhang, *ACS Appl. Mater. Interfaces*, **2020**, 12, 37006–37012.
[14] H. J. Song, H. Yoon, B. Ju, D. W. Kim, *Adv. Energy Mater.*, **2021**, 11, 2002428.
[15] X. Liang, L. Shi, Y. Liu, H. Chen, R. Si, W. Yan, Q. Zhang, G. D. Li, L. Yang, X. Zou, *Angew. Chem. Int. Ed.*, **2019**, 58, 7631–7635.
[16] L. A. She, G. Q. Zhao, T. Y. Ma, J. Chen, W. P. Sun, H. G. Pan, *Adv. Funct. Mater.*, **2022**, 32, 2108465.
[17] L. An, C. Wei, M. Lu, H. Liu, Y. Chen, G. G. Scherer, A. C. Fisher, P. Xi, Z. J. Xu, C. H. Yan, *Adv. Mater.*, **2021**, 33, 2006328.
[18] L. Yang, G. Yu, X. Ai, W. Yan, H. Duan, W. Chen, X. Li, T. Wang, C. Zhang, X. Huang, J. S. Chen and X. Zou, *Nat. Commun.*, **2018**, 9, 5236.
[19] Y. Ping, R. J. Nielsen, W. A. Goddard, 3rd, *J. Am. Chem. Soc.*, **2017**, 139, 149–155.
[20] H. N. Nong, T. Reier, H.-S. Oh, M. Gliech, P. Paciok, T. H. T. Vu, D. Teschner, M. Heggen, V. Petkov, R. Schlögl, T. Jones, P. Strasser, *Nat. Catal.*, **2018**, 1, 841–851.
[21] L. C. Seitz, C. F. Dickens, K. Nishio, Y. Hikita, J. Montoya, A. Doyle, C. Kirk, A. Vojvodic, H. Y. Hwang, J. K. Norskov, T. F. Jaramillo, *Science*, **2016**, 353, 1011–1014.
[22] Q. Qin, H. Jang, Y. M. Wang, L. J. Zhang, Z. J. Li, M. G. Kim, S. G. Liu, X. E. Liu, J. Cho, *Adv. Energy Mater.*, **2021**, 11, 2003561.
[23] J. Gao, C. Q. Xu, S. F. Hung, W. Liu, W. Cai, Z. Zeng, C. Jia, H. M. Chen, H. Xiao, J. Li, Y. Huang, B. Liu, *J. Am. Chem. Soc.*, **2019**, 141, 3014–3023.
[24] J. Ruiz Esquius, D. J. Morgan, G. Algara Siller, D. Gianolio, M. Aramini, L. Lahn, O. Kasian, S. A. Kondrat, R. Schlogl, G. J. Hutchings, R. Arrigo, S. J. Freakley, *J. Am. Chem. Soc.*, **2023**, 145, 6398–6409.
[25] D. F. Abbott, D. Lebedev, K. Waltar, M. Povia, M. Nachtegaal, E. Fabbri, C. Coperet, T. J. Schmidt, *Chem. Mater.*, **2016**, 28, 6591–6604.
[26] A. Loncar, D. Escalera-Lopez, S. Cherevko, N. Hodnik, *Angew. Chem. Int. Ed.*, **2022**, 61, e202114437.
[27] S. Geiger, O. Kasian, M. Ledendecker, E. Pizzutilo, A. M. Mingers, W. T. Fu, O. Diaz-Morales, Z. Z. Li, T. Oellers, L. Fruchter, A. Ludwig, K. J. J. Mayrhofer, M. T. M. Koper, S. Cherevko, *Nat. Catal.*, **2018**, 1, 508–515.
[28] S. Cherevko, S. Geiger, O. Kasian, N. Kulyk, J.-P. Grote, A. Savan, B. R. Shrestha, S. Merzlikin, B. Breitbach, A. Ludwig, K. J. J. Mayrhofer, *Catal.Today*, **2016**, 262, 170–180.
[29] J. Wang, H. Yang, F. Li, L. Li, J. Wu, S. Liu, T. Cheng, Y. Xu, Q. Shao, X. Huang, *Sci. Adv.*, **2022**, 8, eabl9271.
[30] J. Li, L. Zheng, B. Huang, Y. Hu, L. An, Y. Yao, M. Lu, J. Jin, N. Zhang, P. Xi, C. H. Yan, *Small*, **2022**, 18, 2204723.
[31] A. Govind Rajan, E. A. Carter, *Energy Environ. Sci.*, **2020**, 13, 4962–4976.
[32] F. Zhao, B. Wen, W. Niu, Z. Chen, C. Yan, A. Selloni, C. G. Tully, X. Yang, B. E. Koel, *J. Am. Chem. Soc.*, **2021**, 143, 15616–15623.
[33] H. Jin, X. Liu, P. An, C. Tang, H. Yu, Q. Zhang, H. J. Peng, L. Gu, Y. Zheng, T. Song, K. Davey, U. Paik, J. Dong, S. Z. Qiao, *Nat. Commun.*, **2023**, 14, 354.
[34] S. Hao, M. Liu, J. Pan, X. Liu, X. Tan, N. Xu, Y. He, L. Lei, X. Zhang, *Nat. Commun.*, **2020**, 11, 5368.
[35] S. Hao, H. Sheng, M. Liu, J. Huang, G. Zheng, F. Zhang, X. Liu, Z. Su, J. Hu, Y. Qian, L. Zhou, Y. He, B. Song, L. Lei, X. Zhang, S. Jin, *Nat. Nanotechnol.*, **2021**, 16, 1371–1377.
[36] F. Amano, Y. Furusho and Y.-M. Hwang, *ACS Appl. Energy Mater.*, **2020**, 3, 4531–4538.
[37] X. Wang, Y. Tuo, Y. Zhou, D. Wang, S. Wang, J. Zhang, *Chem. Eng. J.*, **2021**, 403, 126297.
[38] J. Wang, B. Ding, X. D. Hao, Y. L. Xu, Y. Wang, L. F. Shen, H. Dou, X. G. Zhang, *Carbon*, **2016**, 102, 255–261.
[39] M. B. Stevens, L. J. Enman, A. S. Batchellor, M. R. Cosby, A. E. Vise, C. D. M. Trang, S. W. Boettcher, *Chem. Mater.*, **2016**, 29, 120–140.
[40] J. Shan, C. Ye, S. Chen, T. Sun, Y. Jiao, L. Liu, C. Zhu, L. Song, Y. Han, M. Jaroniec, Y. Zhu, Y. Zheng, S. Z. Qiao, *J. Am. Chem. Soc.*, **2021**, 143, 5201–5211.
[41] C. C. McCrory, S. Jung, J. C. Peters, T. F. Jaramillo, *J. Am. Chem. Soc.*, **2013**, 135, 16977–16987.
[42] W. Jia, J. Fu, Z. Cao, L. Wang, X. Chi, W. Gao, L.-W. Wang, *J. Comput. Phys.*, **2013**, 251, 102–115.
[43] W. Jia, Z. Cao, L. Wang, J. Fu, X. Chi, W. Gao, L.-W. Wang, *Comput. Phys. Comm.*, **2013**, 184, 9–18.
[44] J. P. Perdew, K. Burke, M. Ernzerhof, *Phys. Rev. Lett.*, **1996**, 77, 3865–3868.
[45] S. Grimme, *WIRs Comput. Mol. Sci.*, **2011**, 1, 211–228.
[46] S. Grimme, J. Antony, S. Ehrlich, H. Krieg, *J. Chem. Phys.*, **2010**, 132, 154104.
[47] S. Grimme, S. Ehrlich, L. Goerigk, *J. Comput. Chem.*, **2011**, 32, 1456–1465.
[48] M. Elmaalouf, M. Odziomek, S. Duran, M. Gayrard, M. Bahri, C. Tard, A. Zitolo, B. Lassalle-Kaiser, J. Y. Piquemal, O. Ersen, C. Boissiere, C. Sanchez, M. Giraud, M. Faustini, J. Peron, *Nat. Commun.*, **2021**, 12, 3935.
[49] S. Czioska, A. Boubnov, D. Escalera-Lopez, J. Geppert, A. Zagalskaya, P. Röse, E. Saraçi, V. Alexandrov, U. Krewer, S. Cherevko, J.-D. Grunwaldt, *ACS Catal.*, **2021**, 11, 10043–10057.
[50] Y. Wang, R. Yang, Y. Ding, B. Zhang, H. Li, B. Bai, M. Li, Y. Cui, J. Xiao, Z. S. Wu, *Nat. Commun.*, **2023**, 14, 1412.
[51] H. Chen, L. Shi, K. Sun, K. Zhang, Q. Liu, J. Ge, X. Liang, B. Tian, Y. Huang, Z. Shi, Z. Wang, W. Zhang, M. Liu, X. Zou, *ACS Catal.*, **2022**, 8658–8666.

# 高价金属钽掺杂无定型氧化铱用于酸性氧析出反应

张　宁[a,b], 杜家毅[a,b], 周　纳[a,b], 王德鹏[a,b], 鲍　迪[a,*], 钟海霞[a,b,*], 张新波[a,b,*]
[a]中国科学院长春应用化学研究所, 稀土资源利用国家重点实验室, 吉林长春130022
[b]中国科学技术大学应用化学与工程学院, 安徽合肥230026

**摘要**: 氢能作为一种潜在的能源载体, 有望取代化石燃料, 解决当今社会的能源需求和环境问题. 质子交换膜电解水(PEMWE)技术因其工作电流密度大、氢气纯度高和系统响应迅速等优点, 能够有效地弥补可再生能源波动性等缺点, 被认为是一种利用可再生能源制氢的可持续手段. 但其阳极氧析出反应(OER)为四电子/质子转移过程, 反应动力学缓慢, 同时强氧化性和强酸性环境会对阳极催化剂的产生腐蚀, 导致稳定性差, 因此亟需开发高效且稳定的催化剂. 研究发现, 无定

型氧化铱材料中的特殊缺陷结构可显著提升其催化酸性OER的活性, 但该结构也会加速反应过程中铱的溶解, 导致催化剂稳定性降低, 严重限制了其实际应用.

本文采用高价金属掺杂的策略, 利用高价金属元素与氧的强成键作用, 对无定型氧化铱的整体结构及活性位点起到优化且稳定的作用. 首先, 采用改性的亚当斯熔融法制备了金属钽掺杂的无定型氧化铱: 350-Ta@$IrO_x$, 400-Ta@$IrO_x$, 450-Ta@$IrO_x$(350, 400和450代表样品分别在350, 400和450 °C烧结), 并用于催化酸性OER; 作为对比, 制备了无掺杂的无定型氧化铱: 350-$IrO_x$, 400-$IrO_x$和450-$IrO_x$. 然后, 通过扫描电子显微镜、透射电子显微镜(TEM)和X射线衍射等表征技术考察了材料的宏观形貌及微观结构. 结果表明, 掺杂后的350-Ta@$IrO_x$材料表面具有丰富的氧空位贡献的活性位点, 且表现出多晶的超小纳米颗粒形貌. 电化学测试结果表明, 350-Ta@$IrO_x$具有较好的酸性OER活性, 在10 mA $cm^{-2}$的电流密度下, 过电势仅为223 mV, 在1.55 V *vs*. RHE的电位下质量活性为1207.4 A $g_{Ir}^{-1}$, 是商业二氧化铱的147.7倍. 且该催化剂的稳定性比未掺杂Ta样品及商业二氧化铱有明显提升, 在0.5 mol $L^{-1}$硫酸溶液中反应500 h后电位未发生明显变化. 密度泛函理论计算结果表明, Ta掺杂与构建缺陷有利于OER决速步中水分子的亲核进攻, 从而提升催化活性并降低反应过电势. 为进一步研究材料在酸性OER工作状态下具有较好稳定性的原因, 采用TEM和X射线光电子能谱等对反应前后的材料进行表征. 结果表明, 350-Ta@$IrO_x$在反应前后结构保持稳定, Ir溶解速率较未掺杂样品明显降低, 证明了Ta掺杂大大提升了无定型氧化铱材料的稳定性.

综上, 本文发展了制备高价金属掺杂氧化铱的改性亚当斯熔融法, 利用高价金属元素与氧的强成键作用, 调控了铱活性位点的电子结构, 同时提升了氧化铱类材料在酸性氧析出反应中的活性与稳定性, 简化了此类材料的合成方式, 为进一步降低质子交换膜电解水器件阳极催化剂的成本和提高其催化活性提供了新思路.

**关键词**: 酸性析氧反应; 高价金属掺杂; 氧化铱; 氧缺陷; 电催化

收稿日期: 2023-05-30. 接受日期: 2023-09-06. 上网时间: 2023-10-25.

*通讯联系人. 电子信箱: xbzhang@ciac.ac.cn (张新波), hxzhong@ciac.ac.cn (钟海霞), dbao@ciac.ac.cn (鲍迪).

基金来源: 国家重点研发计划(2020YFE0204500); 国家自然科学基金优秀青年科学基金项目(海外), 国家自然科学基金(52071311, 52273277, 52072362, 21905269); 吉林省科技发展计划资助项目(20220201112GX); 中国科学院青年创新促进会(2021223).